Tidal Changes on Computed Tomography and Progression of ARDS

Maurizio Cereda, Yi Xin, Hooman Hamedani, Giacomo Bellani, Stephen Kadlecek, Justin Clapp, Luca Guerra, Natalie Meeder, Jennia Rajaei, Nicholas J. Tustison, James C. Gee, Brian P. Kavanagh, Rahim R. Rizi.

Online Supplementary Material

Animal Preparation and Lung Injury

Studies were performed on male Sprague-Dawley rats, with approval by the local Institutional Animal Care and Use Committee (Philadelphia, PA). General anesthesia was induced and maintained with intraperitoneal pentobarbital (40–60 mg/kg initially, 10-20 mg/kg hourly for maintenance), the trachea intubated (14-gauge catheter; BD, Franklin Lakes, NJ), and the glottis sealed (DAP Products Inc., Baltimore, MD) to prevent gas leakage.[1] Paralysis was obtained with pancuronium bromide (1 mg/kg IV; Abbot Labs, North Chicago, IL) injected through a 24 GA tail vein catheter. Rats also received carotid artery catheterization with a 24 GA catheter for arterial blood pressure monitoring and blood gas measurements. Animals were maintained supine throughout the whole study and were ventilated by a small animal ventilator developed in the authors' laboratory.[2] Positive end expiratory pressure (PEEP) was generated by connecting the expiratory gas line to a graduated water column. Airway pressure was continuously recorded using a fiber-optic sensor (Samba Sensors AB, Sweden), and heart rate and peripheral oxygen saturation (SpO_2) levels were monitored by a veterinary pulse-oximeter (Nonin Medical, Inc. Plymouth, MN) attached to the hind foot. Peak inspiratory airway pressures (PIP), plateau pressure (P_{PLAT}), tidal volume (V_T), inspiratory driving pressure (ΔP),[3] and dynamic compliance ($C_{dyn}= \frac{V_T}{PIP-PEEP}$) were recorded. In addition, mechanical power of inspiration [4] was calculated from airway pressure tracings for the whole respiratory system (lung and chest wall). All animals received subcutaneous (30 ml/kg) hydration with normal saline after induction of anesthesia; intravenous saline (10 ml/kg) was administered up to a maximum of three times when the mean arterial blood pressure was lower than 40 mmHg. A rectal probe was used to monitor the animal's body temperature, which was carefully maintained at 37 °C by a heated pad (Gaymar Industries, Orchard Park, NY) placed under the body. After the last set of

measurements, animals were removed from the scanner and euthanized by lethal pentobarbital injection. Hydrochloric acid (HCl) with pH 1.25 was injected through the endotracheal tube at doses ranging between 1 and 4 ml/kg. HCl was injected in two aliquots with the animal in the right and left lateral positions and 45° head elevation. Rats were immediately returned to the supine position and allowed to stabilize while ventilated with PEEP 10 cm H_2O and V_T 6 ml/kg for one hour. No effort was made to spread the liquid in the airways. After stabilization, rats were ventilated with the assigned V_T, PEEP, and respiratory rate, which were not modified throughout the rest of the experiment. All rats received FiO_2 1.0. Rats that survived for at least three hours after stabilization were considered survivors.

Animal Imaging

High resolution whole lung computed tomography (CT) was performed hourly at each time point using a commercial microCT scanner (eXplore CT120 system, Gamma Medica, Inc., Northridge, CA). The lungs were easily contained within the default field of view (85 mm transaxial diameter). Settings used for imaging were: 80 kVp, 32 mA, 16 ms exposure time, 220 projections (half-scan), and 200 µm isotropic resolutions. Imaging was ventilator-gated and performed during 500-ms breath-holds at end inspiration (EI) and end-expiration (EE). Only a single view per breath was acquired during each breath-hold.

Image Analysis

The methodology of CT analysis was designed to spatially match baseline density changes due to lung inflation with the later progression of lung injury. To measure regional inflation at each time point, EI and EE images were registered (superimposed on each other), so that inspiratory

density changes could be assessed in individual voxels. This was accomplished with parametric response map methodology (described below). To measure progression, all serially acquired images were aligned: voxels with increasing density over time could be identified and counted.

Image Registration: The entire scheme of image registration is shown in **Figure 1**. This registration pipeline was implemented using the open source ANTS package with newly refactored Insight Toolkit (version 4).[5] We performed a two-step registration for each pair of EI and EE images; all the subsequent time points for each animal were then registered to the baseline (after HCl aspiration) EI image. The first step of registration was the computation of a rigid transform to coarsely align images by registering the bone structures, using the mutual information as similarity function. The second step consisted of a deformable registration using the symmetric diffeomorphic transformation model [6, 7] with third-order B-spline regularization.[7] Normalized cross correlation was used as the similarity metric between reference and target images.

Image Segmentation: Lung outlines were semi-automatically segmented (separated) from surrounding tissue (i.e. chest wall, diaphragm, the mediastinum). For this purpose, the mask of the baseline EI image (after HCl) was manually outlined by a trained operator and applied to all the subsequent EI and EE images of that same animal, which had been previously registered to the same coordinates. Implementation details and software code of the registration and the procedure of manual segmentation can be found in.[8]

Quality of the Registration Methodology: **Figure 2** shows a representative example of the output of the registration pipeline. Starting from paired EI and EE CT acquisitions, a warped expiratory map (middle panel) was obtained by registering the original EE to the EI image. In the warped

EE image, the bone structure and the major airways appeared to be aligned with the EI image, and the local distribution of aeration was maintained as in the original. To validate alignment of major anatomical structures, we randomly selected 15 rats providing a total of 75 pairs (five time points for each rat) of co-registered EI and EE images and 60 pairs of longitudinally co-registered (between baseline and each subsequent time points) EI images. In each pair, eight anatomic landmarks were chosen at bifurcations of major airway branches.[9] Trained operators manually recorded the spatial coordinates of each landmark, and compared the topological distance in each paired set of co-registered images. The results of the landmark validation of the registration process are shown in **Figure 3**. All operator-labeled landmarks (insert) were in positions that matched reasonably well between EI and warped EE images, with average distance of 325.7±170.4 μm between the corresponding landmarks in each pair. In longitudinal CT acquisitions, landmark positions were also maintained in the warped EI images and the average distance was of 335.7±168.0 μm between markers in the original and in the warped EI images. These distances were not different between landmarks and image acquisitions ($p>0.05$ by ANOVA for all comparisons). **Figure 4** shows examples of displacement fields in healthy and injured rats. These were extracted from the transform functions used to align EE to EI images during the registration process. The color intensity represents the amount of deformation that lung regions underwent during inflation, while the segments indicate its direction. The maps show patterns of deformation that were compatible with physiology, in both healthy and injured lungs. Finally, comparisons of density distributions were performed between the original and the warped images, in both the whole lung and in horizontal bins (**Table 1**). Warping adapts the EE image to fit the size and shape of the EI image, but the percentage of voxels allotted to each density range (as a fraction of total voxels in each image) remained unchanged between warped

and original images (P>0.05 by ANOVA). This confirms that no tissue type was over-represented at the expense of the others, suggesting that distortion artifacts were minimal and percent inflation abnormalities (e.g. atelectasis, mixed aeration) were preserved during image processing.

Parametric Response Mapping: We analyzed lung inflation and injury progression in a voxel-wise manner using parametric response maps (PRM) [10] of all co-registered and segmented images. For this purpose, the frequency distributions of the CT densities of all paired EI and EE voxels were plotted on an equally spaced bi-dimensional 110 by 110 matrix with range between -1000 and 100 Hounsfield Units (HU), then binned in 100 HU increments. Voxels with both EI and EE densities higher than -300 HU were categorized as *severe injury* based on our preliminary and published results showing more severe inflammation in these regions. Changes in the distribution of paired CT density values between two consecutive PRMs (at one hour increments) were then studied. At any given time point, injury progression was considered present if both EI and EE voxel density increased to the -300 HU cut point for severe injury in the later PRM. This binary outcome was categorized for subsequent analysis as '1' where density was -300 HU or greater, and '0' when density did not reach -300 HU.

Risk Quantification: We tested the performance of PRM as a diagnostic tool in identifying the tissue at higher risk of later progression by analyzing range-wise receiver operating characteristic (ROC) [11] between each two consecutive PRMs (one hour apart). We used the density boundaries of each range (100 HU increments) to generate two-dimensional bins in PRM plane (**Figure 5**). These bins were then tested as a dichotomic classifier of propagation vs. stable density as follows: in each PRM we determined the fraction of voxels that showed *injury progression* in the subsequent PRM (after one hour); values of sensitivity and specificity for such

observed progression were calculated for each bin (two dimensional ranges of HU for EE and EI) and averaged for all rats **(Figure 5)**. The averages were weighted by the bin-wise frequency distribution of voxels in the overall population, to assure that bins with high sensitivity and specificity for propagation but containing small numbers of voxels had limited undue influence on the assessment of the bin's overall prediction. A domain of voxels at *high risk* of increasing their density to the *severe injury* region of the PRM after one hour was then identified, where both the sensitivity and the specificity of the prediction (after averaging and normalization) were higher than 0.85 in that bin. Percent values of *high risk* and *severe injury* tissue, measured using PRM in healthy rats are shown in **Table 2**.

Prediction Model: We used a multivariate linear regression model to predict the progression of lung injury from the baseline lung CT densities, i.e. based on the percentage of voxels that fell in the high risk (P_r) and in the severe injury (P_i) domains. In the first stage of model building, each pair of Ei and EE images was used individually to correlate P_r and P_i at baseline with the voxel distribution in the following time point. All the rats (n=73) were used in the training/test model, with all the paired time points one hour apart included resulting in a total of 220 sets of images. All pairs of datasets were treated independently of time acquisition, thus no adjustment for longitudinal correlation was performed. This is justified by the fact that the inclusion of time post-injury as an independent predictor did not significantly improve the model (based on Akakie Information Criterion). A linear regression model containing P_r and P_i, their quadratic terms (P_r^2 and P_i^2), and the interaction of the two terms (P_r*P_i) with logarithmic transformation was used to predict P_r and P_i in the next time point (**Figure 7**). For validation of the prediction model, a jack-knifing cross-validation strategy was used (leave-one out).[12] This approach to validation was chosen due to the heterogeneity of injury trajectory in the sample population. The

residuals of the model were tested to assure the quality of the prediction. Then, we tested whether or not the model generated in the first stage was able to predict voxel distributions in the following time intervals larger than one hour. For this purpose, P_r and P_i in the baseline (after HCl) condition of each rat were used to obtain predicted values of P_r (P_r') and P_i (P_i') after one hour; these predicted values were then used to predict P_r'' and P_i'' after two hours, with an iteration that was continued until the last image of each series. Derived P_r'* and P_i'* values for the final time point of each experiment were then correlated with the actual measured P_r and P_i for validation: a jack-knifing cross-validation strategy was again used, similar to the first stage. Using regression analysis, we then tested whether baseline P_r predicted subsequent worsening of dynamic respiratory compliance (C_{dyn}) and of driving pressure.

Human Imaging: CT images were acquired from a previously published human study on lung metabolism in ARDS.[13] Of a total of 13 patients, we chose 9 subjects who underwent inspiratory and expiratory CT within one week after intubation. A PET/CT tomograph (GE Discovery ST, axial field of view 15 cm, 47 sections 3.27 mm thick), equipped with an 8-slice CT, was used. A section of thorax 15 cm long on the longitudinal axis was acquired, selected on the scout view. In all patients the most cranial slice was above the carina and the most caudal slice below the diaphragmatic dome. One 15 cm long field of view in this region includes approximately 73 % of the lung volume. The images used for the current study were spiral CT scans obtained while holding the airway pressure constant at PEEP, at EI (plateau pressure), and at a pressure equivalent to the mean airway pressure recorded during ventilation (CT fusion). The rotation speed was 0.7 second, with 80 mA, 140 kV, Pitch 1.675 and collimation 1.25*8. Images were reconstructed to voxel size of 0.98*0.98*1 mm (matrix size 512*512, slice thickness = 3.75 mm) with standard Filtered Back Projection FBP. The dosage for each scan was

1.4 mSv. For the current study, inspiratory and expiratory images were registered, manually segmented by trained operators, and replotted in PRM using the same methodology used for the animal scans. High risk and severely injured voxels were identified and measured using the inspiratory-expiratory density ranges derived from the animal experiments. In addition to PRM analysis, CT density analysis was performed, using methods described in the original publication.[13] Briefly, three dimensional regions of interest (ROI) were segmented on the original CT fusion images and partitioned in air and tissue, allowing quantifying lung weight and gas volumes. Tidal recruitment (the weight of lung that collapses and reopens after each inspiration) was also calculated.[13] Results of this analysis are shown in **Table 3**.

Statistical Analysis: Image analysis was performed using Matlab R2013a software (Mathworks) applications developed in the authors' laboratory; statistical analysis was performed using "R" (R Foundation for Statistical Computing; Vienna Austria, http://www.R-project.org). The primary outcome of the analysis was the increase of the fraction of 'severe injury' voxels observed during mechanical ventilation. Comparisons between predicted and measured percent values of high-risk or severely injured voxels were performed using linear regression; the agreement between variables was tested using Bland-Altman plots [14] and by calculating the 95% limits of agreement (LOA). ANOVA with Bonferroni correction was used for intergroup comparisons and to compare landmark between images. An α of 0·05 was used for type I error. All data were expressed as mean ± standard deviation.

References

1. Cereda M, Emami K, Xin Y, et al. Imaging the interaction of atelectasis and overdistension in surfactant-depleted lungs. Critical Care Medicine 2013;**41**(2):527-35 doi: 10.1097/CCM.0b013e31826ab1f2; 10.1097/CCM.0b013e31826ab1f2[published Online First: Epub Date]|.
2. Spector ZZ, Emami K, Fischer MC, et al. A small animal model of regional alveolar ventilation using HP 3He MRI1. Academic Radiology 2004;**11**(10):1171-79 doi: 10.1016/j.acra.2004.08.001[published Online First: Epub Date]|.
3. Amato MB, Meade MO, Slutsky AS, et al. Driving pressure and survival in the acute respiratory distress syndrome. N Engl J Med 2015;**372**(8):747-55 doi: 10.1056/NEJMsa1410639[published Online First: Epub Date]|.
4. Cressoni M, Gotti M, Chiurazzi C, et al. Mechanical Power and Development of Ventilator-induced Lung Injury. Anesthesiology 2016;**124**(5):1100-8 doi: 10.1097/ALN.0000000000001056[published Online First: Epub Date]|.
5. Avants BB, Tustison NJ, Stauffer M, Song G, Wu B, Gee JC. The Insight ToolKit image registration framework. Frontiers in neuroinformatics 2014;**8**:44 doi: 10.3389/fninf.2014.00044[published Online First: Epub Date]|.
6. Avants BB, Epstein CL, Grossman M, Gee JC. Symmetric diffeomorphic image registration with cross-correlation: evaluating automated labeling of elderly and neurodegenerative brain. Medical image analysis 2008;**12**(1):26-41 doi: 10.1016/j.media.2007.06.004[published Online First: Epub Date]|.
7. Tustison NJ, Avants BB. Explicit B-spline regularization in diffeomorphic image registration. Frontiers in neuroinformatics 2013;**7**:39 doi: 10.3389/fninf.2013.00039[published Online First: Epub Date]|.
8. Xin Y, Song G, Cereda M, et al. Semiautomatic segmentation of longitudinal computed tomography images in a rat model of lung injury by surfactant depletion. J Appl Physiol 2015;**118**(3):377-85
9. Li B, Christensen GE, Hoffman EA, McLennan G, Reinhardt JM. Pulmonary CT image registration and warping for tracking tissue deformation during the respiratory cycle through 3D consistent image registration. Med Phys 2008;**35**(12):5575-83
10. Galban CJ, Han MK, Boes JL, et al. Computed tomography-based biomarker provides unique signature for diagnosis of COPD phenotypes and disease progression. Nat Med 2012;**18**(11):1711-5 doi: 10.1038/nm.2971[published Online First: Epub Date]|.
11. Hanley JA, McNeil BJ. The meaning and use of the area under a receiver operating characteristic (ROC) curve. Radiology 1982;**143**(1):29-36 doi: 10.1148/radiology.143.1.7063747[published Online First: Epub Date]|.
12. Kearns M, Mansour Y, Ng AY, et al. An experimental and theoretical comparison of model selection methods. Machine Learning 1997; **27** (1): 7-50
13. Bellani G, Guerra L, Musch G, et al. Lung regional metabolic activity and gas volume changes induced by tidal ventilation in patients with acute lung injury. Am J Respir Crit Care Med 2011;**183**(9):1193-9 doi: 10.1164/rccm.201008-1318OC[published Online First: Epub Date]|.
14. Bland JM, Altman DG. Statistical Methods for Assessing Agreement between Two Methods of Clinical Measurement. Lancet 1986;**1**(8476):307-10

Table 1. Percent differences (as a fraction of total lung volume) of aeration compartments between warped and original expiratory images. A sample of 70 registered expiratory images was randomly selected from the groups with decreased (5 rats) and stable (5 rats) compliance. The intensity histogram from warped and original images were analyzed globally by separating four compartments, named hyper-aerated [-1000 to -901 HU], normal aerated [-900 to -501 HU], partial aerated [-500 to -101 HU] and non-aerated [-100 to 100 HU]. Furthermore, each three-dimensional image was separated in three anterior to posterior regions. The warped - original gradients were not different between the aeration compartments and between regions of the lung (P>0.05 by ANOVA for all comparisons).

	Tissue Fraction		Warped-Original				Warped-Original		
Decreased Compliance	Hyper Aerated	Global	0.20%	±	0.29%	Anterior	0.01%	±	0.65%
						Middle	0.29%	±	0.15%
						Posterior	0.01%	±	0.57%
	Normal Aerated	Global	0.36%	±	0.27%	Anterior	0.11%	±	0.16%
						Middle	0.47%	±	0.23%
						Posterior	0.45%	±	0.16%
	Partial Aerated	Global	-0.83%	±	0.82%	Anterior	-0.22%	±	0.37%
						Middle	-0.75%	±	0.52%
						Posterior	-1.11%	±	0.34%
	Non Aerated	Global	-0.38%	±	0.45%	Anterior	-0.49%	±	0.17%
						Middle	-0.25%	±	0.15%
						Posterior	-0.44%	±	0.14%
Stable Compliance	Hyper Aerated	Global	0.07%	±	0.15%	Anterior	0.12%	±	0.10%
						Middle	0.04%	±	0.17%
						Posterior	0.20%	±	0.12%
	Normal Aerated	Global	0.07%	±	0.27%	Anterior	0.01%	±	0.11%
						Middle	0.05%	±	0.16%
						Posterior	0.01%	±	0.15%
	Partial Aerated	Global	-0.21%	±	0.55%	Anterior	-0.02%	±	0.40%
						Middle	-0.03%	±	0.22%
						Posterior	-0.52%	±	0.33%
	Non Aerated	Global	-0.09%	±	0.37%	Anterior	0.17%	±	0.24%
						Middle	-0.11%	±	0.26%
						Posterior	-0.03%	±	0.32%

Table 2: Distribution (as percent of total lung volume) of voxels with imaging characteristics of healthy tissue, *high risk* tissue, and *severe injury* (i.e. stable density > -300 HU) in eight healthy rats ventilated with V_T 12 ml/kg and PEEP 3 cmH2O.

	#1	**#2**	**#3**	**#4**	**#5**	**#6**	**#7**	**#8**	**Mean**	**Std**
Healthy Tissue	95.06%	94.44%	94.98%	93.35%	95.20%	96.24%	97.03%	94.37%	95.09%	1.14%
Unstable Inflation	4.75%	5.24%	4.56%	6.20%	4.63%	3.60%	2.91%	5.49%	4.67%	1.04%
Severe Injury	0.19%	0.32%	0.46%	0.45%	0.16%	0.16%	0.05%	0.14%	0.24%	0.15%

Table 3. Imaging characteristics of the nine patients included in the human portion of the study. High risk and severely injured tissue were measured using parametric response mapping in co-registered inspiratory and expiratory images. All other CT parameters were measured on the manually segmented images. All percent values are calculated as % of lung volume. Patients are reported in the same order as in Table 2 of the main text.

#	**High–Risk Tissue [%]**	**Severe Injury [%]**	**Lung volume (liters)**	**Lung weight (grams)**	**Tidal recruitment (ml)**	**Tidal recruitment (%)**
1	35.0	34.9	1.01	1100	29.5	2.9
2	35.4	21.2	1.98	1277	71.2	3.6
3	29.8	32.1	1.55	1094	29.2	1.9
4	27.7	26.1	1.38	1253	74.2	5.4
5	17.7	23.7	2.22	1154	70.8	3.2
6	11.1	29.2	2.42	740	40.2	1.7
7	13.3	24.2	2.32	995	30.2	1.3
8	13.1	19.4	2.04	772	59.8	2.9
9	17.9	43.0	1.33	1307	67.2	5.1

Figure 1. The pipeline of image registration. All the sequential $EI_{(1-4)}$ were registered to EI_0 (the first EI image after acid aspiration), with corresponding transformation function ϕ_{01} ϕ_{02} ϕ_{03} ϕ_{04}. Each pair of EI and EE images was registered with transformation function ϕ_{00} ϕ_{11} ϕ_{22} ϕ_{33} ϕ_{44}. For example the EE image at the fifth hours, denoted EE_4 was registered to EI_0 by utilizing $\phi_{04}\phi_{44}EE_4$.

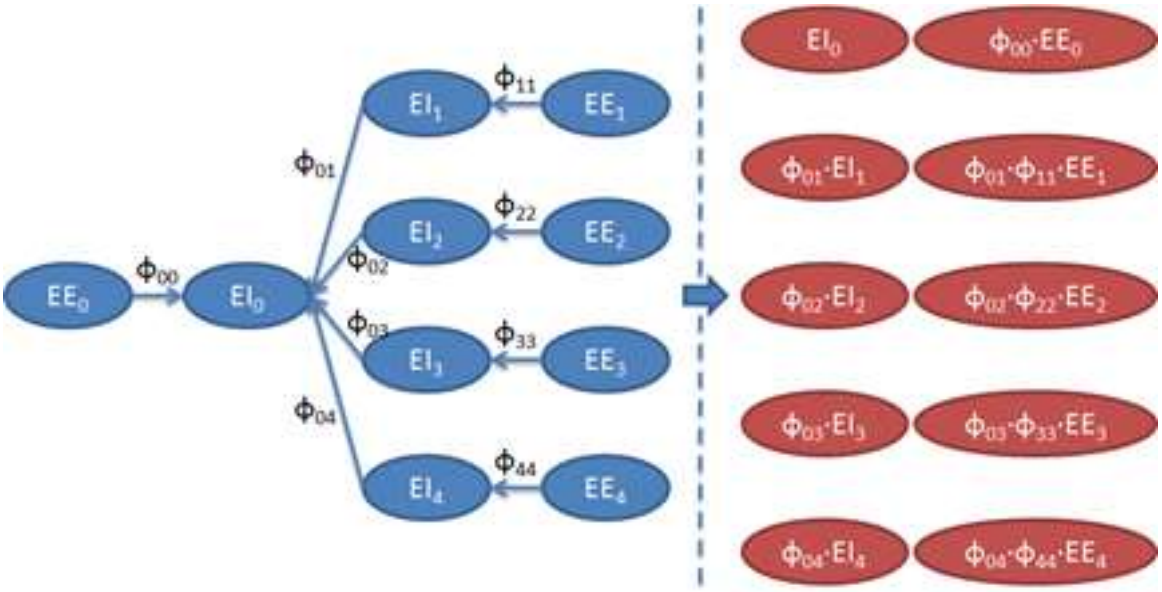

Figure 2. Representative end-inspiratory (EI), and-expiratory (EE), and warped EE images in a rat at baseline (after aspiration of hydrochloric acid). Major airway and bone landmarks are visually matched between EI and warped EE. In the warped EE image, the local distribution of aeration was maintained as in the original EE.

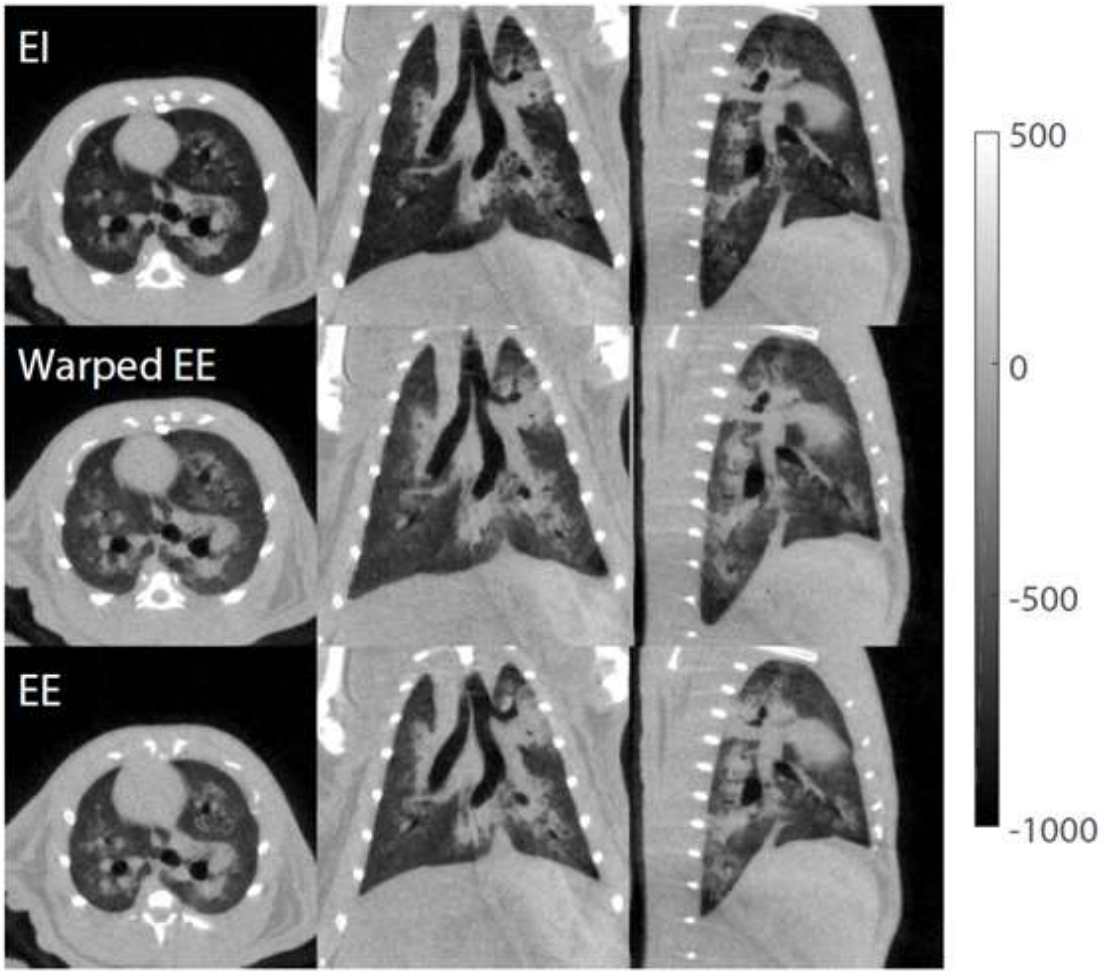

Figure 3. A: Eight anatomic landmarks were chosen at major bifurcations of airway branches in 15 randomly selected rats. B: The topographic distances between markers set in EI and warped EE (○), and in longitudinally co-registered EI images across all available time points (□) are plotted for each landmark (numbered 1-8). Distances were small and unaffected by landmark locations and image acquisitions ($p>0.05$ for all comparisons).

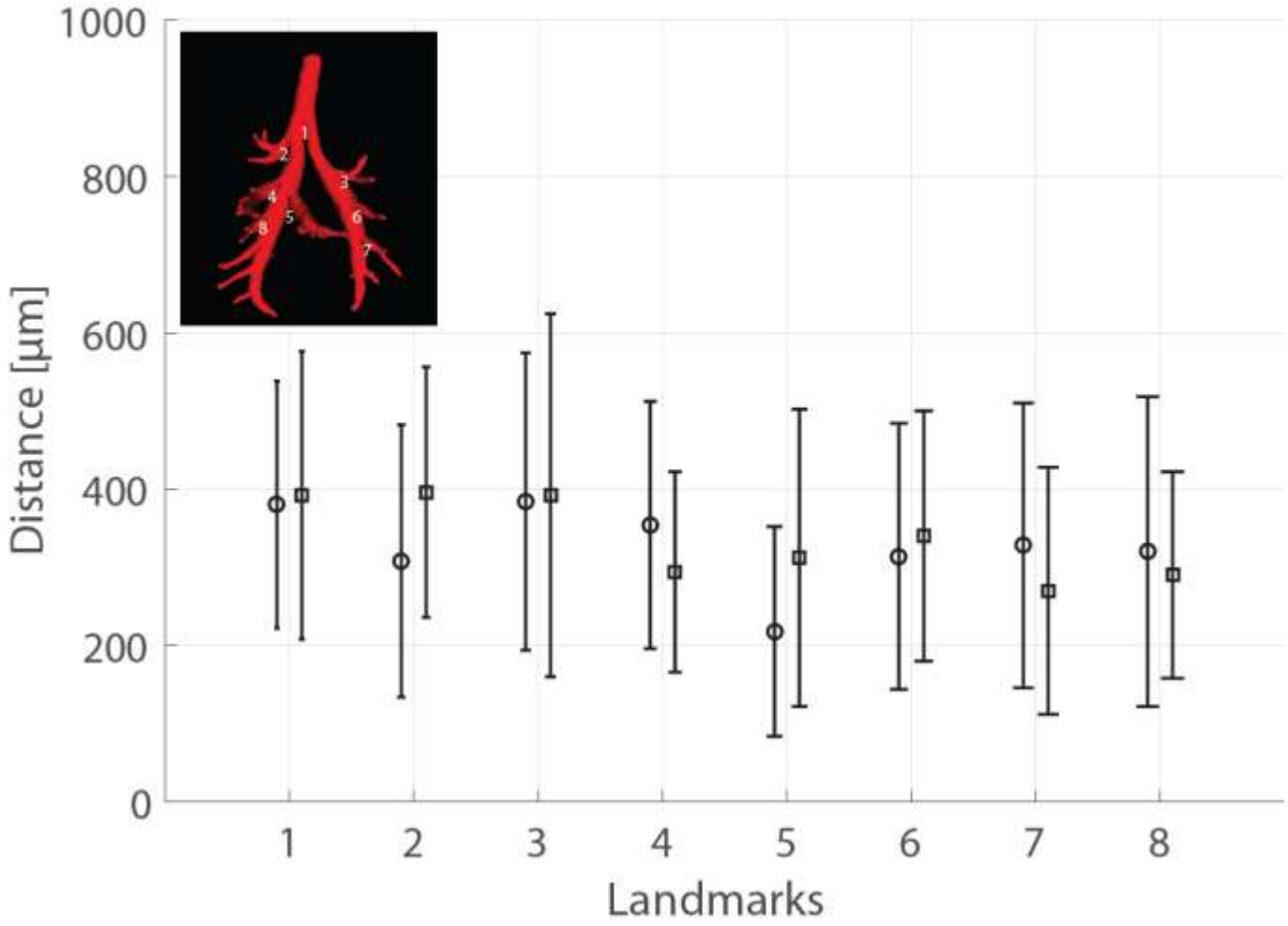

Figue 4. Representative inspiratory and expiratory images of a healthy rat ventilated with PEEP 10 cmH_2O and V_T 6 ml/kg (A), and of an injured rat with PEEP 3 cmH_2O and V_T 12 ml/kg (B). Corresponding displacement field maps, obtained during the registration process are shown (C,D). The displacement vectors (arrows, see zoomed image in C for detailed visualization) represent the displacement of the pixels (distance traveled in mm), the tail and head of each arrow representing the pixel location respectively at inpiration and expiration during tidal breathing. Caudal lung regions (near the diaphragm) had larger displacement as expected. Low PEEP and higher V_T caused larger displacement in the lower lobes (green arrows in D). The injured lung region had larger displacement vectors than the contralateral healthy region (blue arrows in the zoomed image).

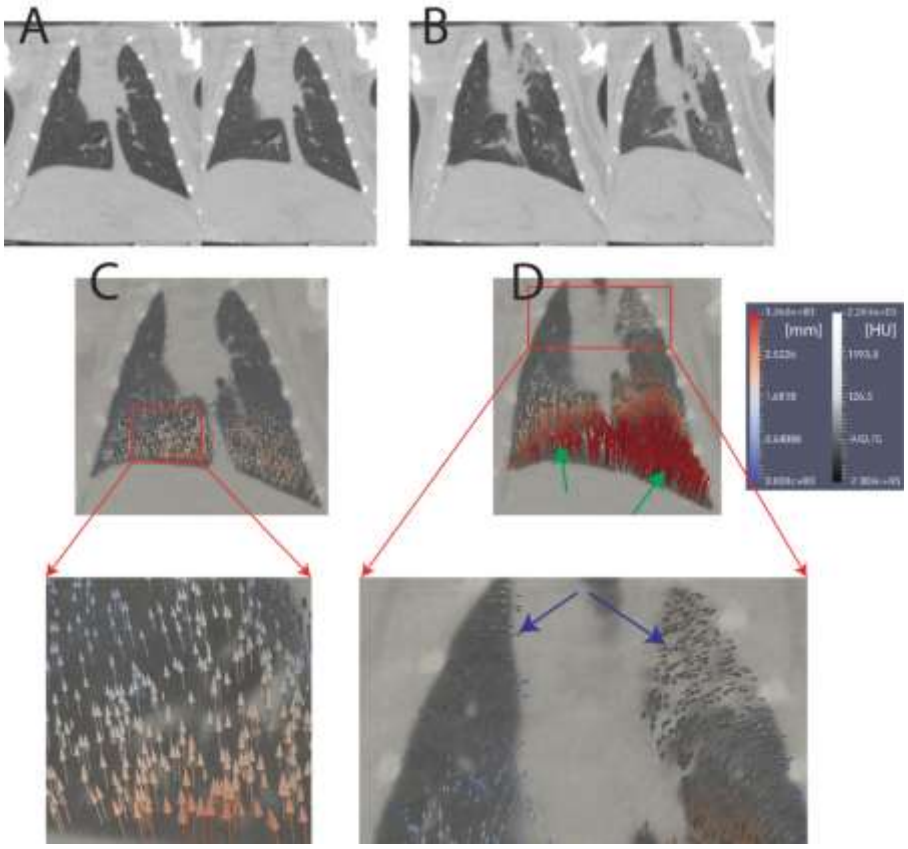

Figure 5. Graphic illustration of the receiver operator characteristic (ROC) analysis applied to parametric response maps. Each PRM was divided in square bins (100 HU wide); in each bin, we then determined the fraction of voxels that progressed to *severe injury* (EI and EE density >-300 HU) in the subsequent PRM (after one hour). Using the boundary of each bin as 'test' for later progression vs. no progression, we calculated values of sensitivity and specificity for such progression in each bin. We averaged these values for all rats and normalized them by the overall frequency distribution of the whole population. Bins in the left lower corner of the PRM (low EI and EE density) have high sensitivity but low specificity as predictors of progression (at lower initial density, the probability of missing progression is low, but many voxels will not progress). In contrast, voxels in the right upper corner (high density) range have high specificity but low sensitivity. Finally, a region at *high risk* of progression was identified by setting an empiric threshold of >0.85 for *both* sensitivity and specificity.

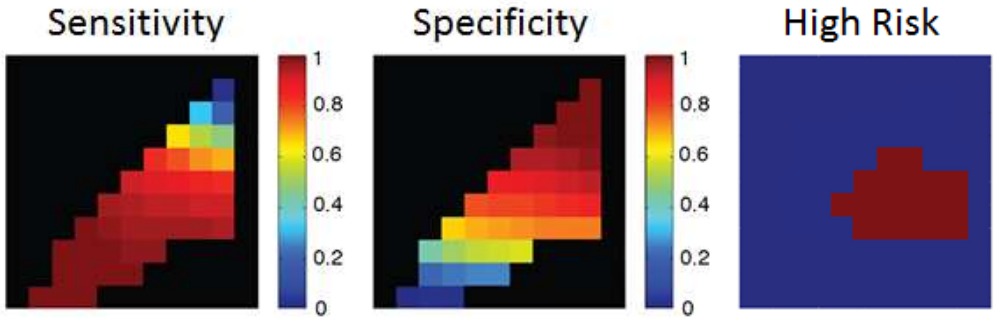

Figure 6. Topographic distances (in 1 mm wide pixels) between anatomical landmarks in EI and warped EE images in humans.

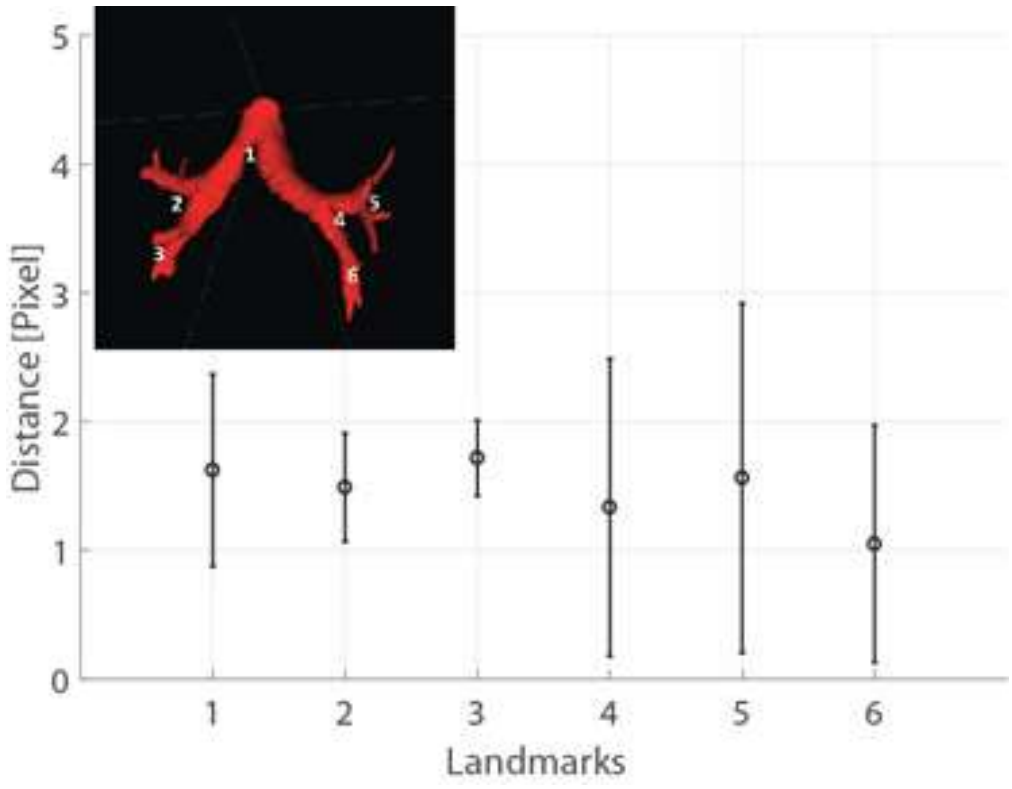

Figure 7. CT density distributions predicted by the model were compared with the true values measured in the corresponding image. Correlations between predicted and measured values at one hour intervals are shown for at risk (A) and severely injured (B) parenchyma.

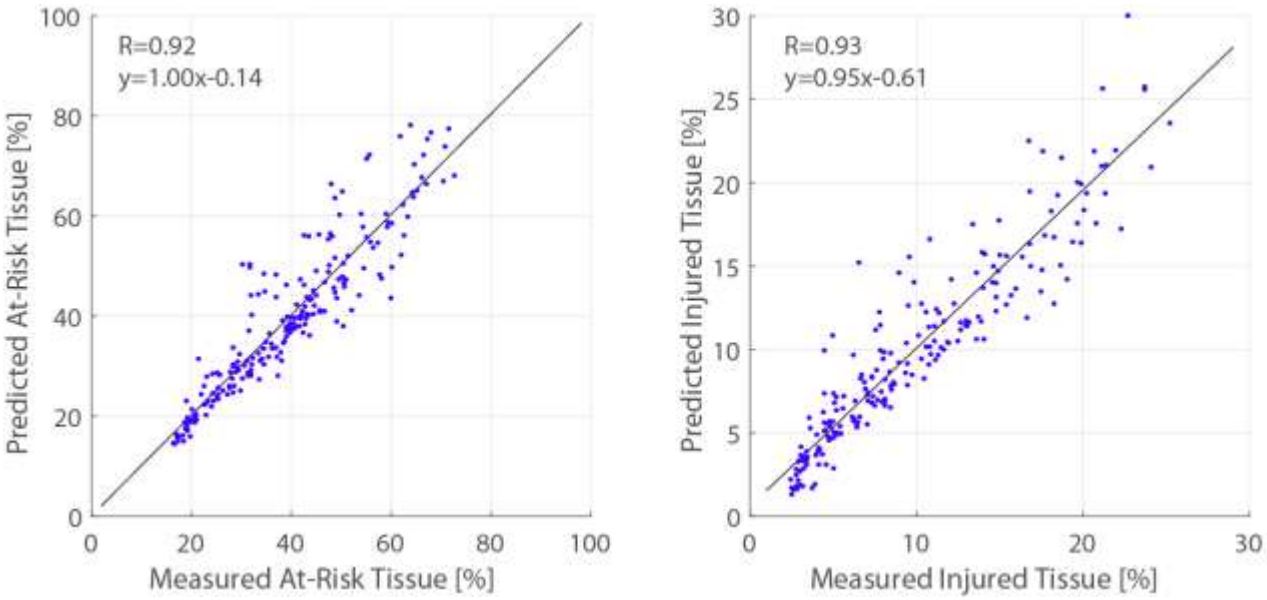

Figure 8: Correlation between the baseline (after HCl) percent fraction of high-risk tissue and the future increase of driving pressure during the course of mechanical ventilation. Red circles: non-protective ventilation group; blue circles: protective ventilation.

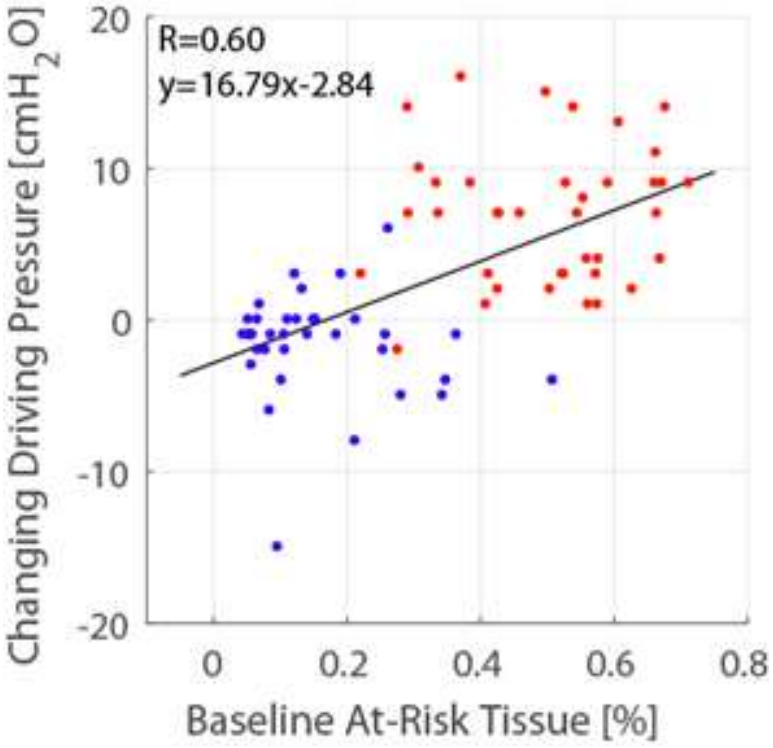

Figure 9. Inspiratory-expiratory computed tomography images of 9 patients with ARDS, 3 non-survivors (top) and six survivors (bottom).